Calcif Tissue Int (2009) 85:434–443
DOI 10.1007/s00223-009-9284-0

Correlation of High-Resolution X-Ray Micro-Computed Tomography with Bioluminescence Imaging of Multiple Myeloma Growth in a Xenograft Mouse Model

Andrei A. Postnov · Henk Rozemuller · Viviene Verwey · Henk Lokhorst · Nora De Clerck · Anton C. Martens

Received: 27 October 2008 / Accepted: 12 August 2009 / Published online: 9 October 2009

Abstract Multiple myeloma (MM) is an incurable B-cell neoplasia in which progressive skeletal lesions are a characteristic feature. Earlier we established an animal model for human MM in the immune-deficient RAG2$^{-/-}\gamma c^{-/-}$ mouse, in which the growth of luciferase-transduced MM cells was visualized using noninvasive bioluminescence imaging (BLI). This model appeared well suited to study disease progression and response to therapy by identifying the location of various foci of MM tumor growth scattered throughout the skeleton and at subsequent time points the quantitative assessment of the tumor load by using BLI. We report here on the corresponding high-resolution X-ray micro-computed tomographic (micro-CT) analysis to study skeletal defects in the mice with full-blown MM. Several anatomical derangements were observed, including abnormalities in geometry and morphology, asymmetrical bone structures, decreased overall density in the remaining bone, loss of trabecular bone mass, destruction of the inner microarchitecture, as well as cortical perforations. Using the combination of BLI, micro-CT imaging, and immune-histopathological techniques, we found a high correlation between the micro-CT-identified lesions, exact tumor location, and infiltration leading to structural lesions and local bone deformation. This confirms that this animal model strongly resembles human MM and has the potential for studying the biology of MM growth and for preclinical testing of novel therapies for MM and for repair of MM-induced bone lesions.

Keywords Micro-CT · Bioluminescence imaging · Human multiple myeloma · Immune-deficient mouse model · Bone lesion

Multiple myeloma (MM) is an incurable B-cell neoplasia, of which one of the characteristics is focal growth of MM cells scattered throughout the skeleton [1]. A typical feature of MM growth in the bone marrow environment in patients is the development of lesions in bone structures caused by secretion of cytokines that, among others, lead to stimulation of osteoclast activity. Effective treatment of MM should therefore not only be directed at inducing a reduction of the tumor but also at inducing repair of the MM-induced bone lesions. Preclinical testing of new therapeutic strategies for the treatment of MM requires animal models that closely resemble human disease in both these aspects. Among murine models the 5T2MM model [2] is highly valued because it strongly mimics human MM growth, including its hallmark of osteolytic lesions that were shown by micro-computed tomography (micro-CT) to result in cortical perforations at the terminal stage of the disease [3]. The murine model is also used not only for unraveling basic biological processes in MM but also for testing of potentially new therapeutic targets [4]. For translational immunotherapy research in a humanized model it is, however, desirable to establish a possible role

The first two authors contributed equally to this work.

A. A. Postnov · N. De Clerck
Department of Biomedical Sciences and Physics, University of Antwerp, Antwerp, Belgium

H. Rozemuller · V. Verwey · A. C. Martens (✉)
Department of Immunology, KC02.085.2, Stem cell Research, and Molecular Imaging, University Medical Center Utrecht, PO Box 85090, Lundlaan 6, 3584EA Utrecht, The Netherlands
e-mail: a.martens@umcutrecht.nl

H. Lokhorst
Department of Hematology, University Medical Center Utrecht, Utrecht, The Netherlands

for minor HLA antigens as targets for MM therapy [5] or for testing MM-specific T-cell clones and the T-cell receptor transfer approach [6]. For preclinical testing of novel treatment strategies a humanized animal model will provide relevant data [7]. There are a limited number of xenograft models of human myeloma in immune-deficient mice, e.g.—SCID mice [8–10], humanized SCID-Hu [11, 12], nonobese SCID mice [13–17], and SCID-Rab [18]—in which several studies are ongoing that are aimed at identifying the illusive MM stem cell which is the ultimate target that has to be eliminated to cure the disease [19]. While these models offer unique opportunities to study the pathobiology of human MM in vivo, they have their limitations for testing new therapeutics against human myeloma because as yet they are not suited for reproducible, convenient, and sensitive monitoring of cytotoxic or immunological therapies. In preclinical animal model research it is important to select the appropriate model for addressing specific research questions [7]. For MM studies this implies having adequate analytical tools to detect and quantify MM tumors and to analyze the typical MM-associated pathological changes in the microenvironment. We therefore developed a humanized murine model for MM in the RAG2$^{-/-}\gamma c^{-/-}$ knock-out (KO) immune-deficient mouse [20], in which we showed that human MM cells can successfully engraft since this mouse strain typically lacks B, T, and NK cells [21, 22]. To monitor the in vivo MM growth quantitatively, we injected RAG2$^{-/-}\gamma c^{-/-}$ mice intravenously with luciferase gene–transduced MM cells. For preclinical development of therapies based on immunological targeting of myeloma cells with humanized antibodies or minor HLA antigen–specific T cells, it is important to use human myeloma cells already in the preclinical phase. Therefore, we used U266 and RPMI 8226/S cell lines, which are both derived from myeloma patients and have extensively been studied. Although the long ex vivo culturing of these cells may have affected typical MM characteristics, they retained the specific behavior of homing only to the bone marrow environment as well as the expression of CD138 [20]. The MM model has been validated for such therapeutic interventions as total-body irradiation and donor lymphocyte infusion, as described earlier [20]. Here, we describe the results of a micro-CT analysis of human MM-induced bone lesions in this model. At sequential time points the outgrowth of MM cells was visualized by noninvasive bioluminescence imaging (BLI) in living mice. Whereas the BLI signal indicates the presence of tumor cells, it does not show in full detail what part of the skeleton is affected nor does it identify the nature of the lesions caused by MM.

For a more focused insight into the defects caused by MM, high-resolution X-ray micro- CT was applied post mortem [23, 24]. Full-body scans were combined with an extensive analysis of isolated bones. Micro-CT imaging allowed exact localization and identification of the anatomical structures that were affected. Abnormalities in geometry, morphology, and asymmetrical bone structures were seen. Also, the ectopic calcification outside the skeleton was detected. A correlation was made between data from micro-CT, presence of MM cells, and BLI to show the potential of the combination of BLI and micro-CT.

Materials and Methods

Cell Lines and Cell Culturing

The human MM cell lines that we describe in this study are U266 and RPMI-8226/S, of human origin (both obtained from the American Tissue Culture Collection [ATCC])—cultured, transduced with the luciferase-GFP gene, and characterized as described earlier [20].

Transplantation of MM Cells into RAG2$^{-/-}\gamma c^{-/-}$ Mice

Immune-deficient mice from the RAG2$^{-/-}\gamma c^{-/-}$ (double KO) strain were used in the experiments at the age of 9–14 weeks. Twenty-four hours before the injection of freshly cultured MM, mice received total-body irradiation (TBI, 3.0 Gy X-rays). MM cells (5×10^6) suspended in 200 µl PBS containing 0.1% BSA (GIBCO, Breda, The Netherlands) were injected intravenously (i.v.) via the lateral tail vein. The tumor load in the mice was determined by weekly BLI measurements as described [20]. In case of paralysis of the hind limbs or when the mice became moribund, the experiment was terminated. The mice were imaged in detail just before being killed by cervical dislocation. Organs and skeletal parts were isolated and fixed in 4% formalin. As controls we killed mice of both sexes at the same age. Organs and the skeleton were isolated and fixed in formalin.

BLI

A few minutes before BLI, the mice were anesthetized by intramuscular (i.m.) injection of 50 µl of ketamine–xylazine–atropine. One minute before imaging, the mice received an intraperitoneal (i.p.) injection of 100 µl 7.5 mM D-luciferine (i.e., 125 mg/kg; Synchem Chemie, Kassel, Germany) and were placed in a light-tight chamber. Bioluminescence images were taken from both the ventral and the dorsal sides of the mice using a cooled charge-coupled device (CCCD) camera (Roper Scientific Princeton Instrument, Trenton, NJ), fitted to a light-tight chamber and mounted with a 50-mm F1.2 Nikon lens, controlled by the MetaVue Software package (Universal Imaging,

Downingtown, PA). The instrument is especially designed for photon counting. The integrated light intensity of a stack of 10 sequential 1-minute exposures was used to quantify the amount of light emitted by the MM cells. A low-intensity visible light image was made and used to produce "overlay" images. The images were analyzed with MetaMorph Imaging System software (Universal Imaging Corporation).

Histopathological Examination

Femurs were fixed, decalcified in saturated EDTA for 7 days, and embedded in paraffin. Sections, 5 μm thick, were stained with hematoxylin and eosin for histological examination. For detection of human MM cells, sections were labeled with anti-CD138 (Labvision, Fremont, CA). As secondary antibody PowerVision Poly HRP-anti Rabbit IgG (ImmunoLogic/Klinpath, Duiven, The Netherlands) was used, followed by the peroxidase enzymatic reaction. CD138 was used because FACS analysis of U266 and RPMI 8226/S cells indicated that MM cells expressed this CD marker in vitro as well as ex vivo in culture; it was used for the in situ detection of foci of CD138-positive MM cells on histological slides [20].

High-Resolution X-Ray Micro-CT

Micro-CT scans were obtained at the end of the experiments after the death of the animals. Initially, in fixed animals the whole skeleton, except for the skull, was scanned in an X-ray micro-CT system (Skyscan 1076, Kontich, Belgium) in order to determine which parts of the skeleton were affected. Both the X-ray source (focal spot size 8 μm, energy range 20–100 keV) and the detector (CCD camera 2.3kx4k) rotated around the animal. Scanning time (12 minutes per scan of an area 18 mm long) and conditions were selected to mimic an in vivo study of the animals described earlier by our group [24]. Pixel size was 35 μm. A 90-kV tube voltage and a Ti filter in the beam path were used. Rotation angle was 0.5°. In total six to eight successive scans (each 18 mm long) were acquired in each animal to visualize the whole skeleton. Eleven diseased and four control animals were scanned.

Based on the evaluation of the initial results of the full-body scans, bones from the MM and control mice were isolated and scanned by high-resolution X-ray micro-CT (Skyscan 1072) with a pixel size of 13 μm. For more detailed CT the right femur and tibia, sternum; pelvic region including sacrum, ileum, sacral, lumbar and thoracic vertebrae were selected for all mice regardless of the BLI signals. From the 11 mice that we studied five to seven specimens were scanned in detail. In this micro-CT set-up, the camera and X-ray source were fixed, while the bones were mounted on a rotating stage. Source parameters were 80 kV and 100 μA. A total of four frames were acquired with a 0.9° rotation step, resulting in a scanning time of about 2 hours. In all scans virtual cross sections were reconstructed by the Feldkamp cone beam algorithm [25]. 3D models were built by Skyscan software. Further details of both scanners were published elsewhere (www.skyscan.be).

Results

Engraftment and Tumor Growth of MM Cell Lines

The cell lines U266 and RPMI-8226/S were selected because they showed a characteristic outgrowth at multiple sites scattered throughout the bone marrow compartment. Following i.v. injection of 5×10^6 MM cells, the first signs of MM growth appeared after 3 weeks, illustrated by focal areas of luciferase activity detected by BLI. The mice were imaged every week, and photon counting of emitted light provided a quantitative parameter to measure tumor load, enabling the construction of tumor growth curves. Figure 1a shows the resulting growth curves for the RPMI-8226/S cell line and Fig. 1b the curves for the U266 MM cell line. Figure 1c, d depicts a representative mouse (number 9), showing the location as well as the subsequent outgrowth from weeks 3 through 15 at the ventral and dorsal sides, respectively. The 2-weekly images show an increase of the various foci with luciferase activity throughout the skeleton of the mouse. As can be seen clearly, the first signs of MM growth are in the femur and tibia, followed by luciferase activity at other locations, e.g., the pelvic region, jaw, ribs, vertebrae, and sternum. The outgrowth of MM tumors appeared to be restricted to the sites of initial homing because in the course of MM development only rarely were new sites of MM growth observed. BLI-negative skeleton parts showed no outgrowth of MM tumors. To show the 2-weekly image in a single figure, we depicted the subsequent images at different scaling to prevent oversaturation of the image (Fig. 1c, d). This is illustrative for the large increase in local tumor load during tumor progression. Toward the terminal phase of the disease we observed emerging hind-leg paralysis in most of the animals, which was the reason to kill the animals and to use them for post mortem micro-CT analyses.

Micro-CT Imaging

Initially, full-body micro-CT revealed the location of anatomical derangements in mice with MM.

A correlation was made between the BLI results and micro-CT scanning of 11 complete skeletons of myeloma-diseased mice. Fifty-one positive BLI signals were detected,

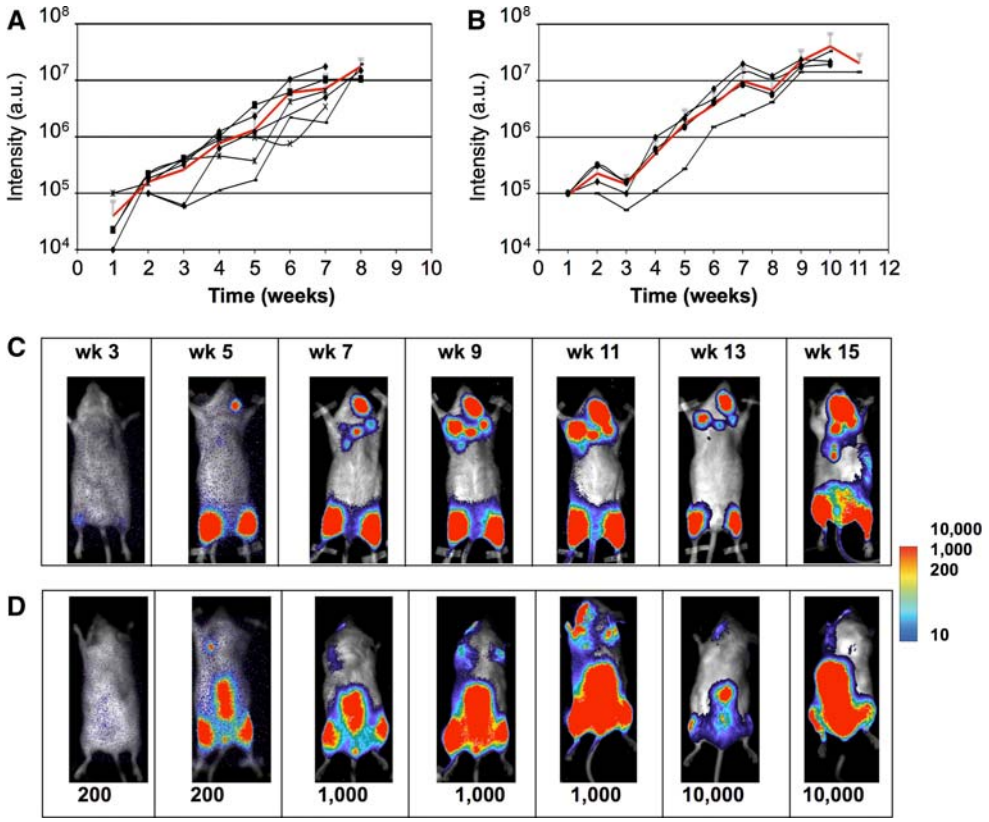

Fig. 1 Growth kinetics of human MM cell lines in individual RAG2$^{-/-}\gamma c^{-/-}$ mice. The increase in luciferase activity in individual mice as a measure of the tumor load is shown: **a** RPMI-8226/S (n = 6), **b** U266 (n = 5). The thick (*red*) line in both graphs represents the mean value from the mice in the respective groups. **c, d** Bioluminescence images from a representative mouse (number 9), taken from the ventral side (**c**) or from the dorsal side (**d**), with 2-week intervals after inoculation of 5 × 10^6 U266 MM cells. Scaling of the images differs between the images taken at different time points, as indicated, in order to visualize all images in a single figure. Images are depicted in false color ranging from *blue* to *red*. For weeks 3 and 5 the number 200 indicates a scaling of the light intensity ranging from 10–200 arbitrary units (a.u.)/pixel for weeks 7, 9, and 11 and the number 1,000 indicates a scaling ranging 10–1,000 a.u./pixel; for weeks 13 and 15 the number 10,000 indicates a scaling ranging 10–10,000 a.u./pixel. (Color figure online)

whereas micro-CT showed that 53 regions in the skeleton were affected. To evaluate the correlation of BLI and micro-CT, we summarized the correlation between the different imaging signals (BLI and micro-CT) in Table 1. For the femora and tibiae, a correlation in 19/22 was observed between the two techniques and in the sternum a correlation in 7/10 (one specimen was excluded due to the inability to make scans of that area). For the pelvic (sacrum) area a correlation was seen in 10/11 specimens examined, whereas only 16/22 of the signals could be matched in the humera. BLI signals in the chest area, especially the ribs, could not be confirmed by micro-CT because these structures are too small on the tomographic slices. It should also be noted that the skull was not included in the micro-CT analysis.

Based on the results of the full-body scans, individual bones were isolated and scanned at 13 µm pixel size. The selected bones were the right femur and tibia, sternum, ileum and sacrum including the sacral vertebrae, and lumbar vertebrae. Results are illustrated by representative examples. Both cortical bone and trabecular bone were visualized in an isolated tibia from a control mouse (Fig. 2a) and a diseased one (Fig. 2b). Figure 2a, b shows virtual tomographic slices. In the MM mouse, trabecular bone mass was reduced and part of the inner microarchitecture of the bone disappeared. Overall density of the remaining bone structures was smaller in diseased mice compared to controls. In Fig. 2c, 3D models were reconstructed. The panel at the left is the control tibia. In the affected bones, arrows indicate cortical perforations. Similar abnormal perforations could be observed in cortical bone other than in the tibia. Osteolytic lesions caused by MM to the vertebrae can be seen in virtual cross sections in control mice (Fig. 3a, b) and in MM mice (Fig. 3c, d). Similar to the tibia, trabecular bone mass is reduced together with the disappearance of the inner microarchitecture. In the diseased mouse, the bone in the vertebrae

Table 1 Correlation of BLI-based localization of foci of MM growth and micro-CT analysis–based anomalies in the skeleton of MM-bearing mice

cell line/ mouse number	code	day of death	L Femur+Tibia	R Femur+Tibia	sternum	sacrum	L humerus	R humerus
RPMI								
1	RPMI-4	54			NS		B	
2	RPMI-5	54						
3	R2	63					B	
4	RPMI-1	48						
5	RPMI24	52	B					
6	RPMI-50/7	50					S	
U266								
7	U266-4	76	B				B	B
8	U266-2 1st	74						
9	U266-5	105			B			
10	U266-2 2nd	105			S		B	
11	U266-II	12			S	S		

All mice received 5×10^6 MM cells at day 0 and developed the disease. BLI signals were only observed in the skeleton. A gray cell in the table indicates a correlation of the occurrence of a BLI signal and the presence of skeletal aberrations in the same bone. "B" in a black cell indicates the presence of a BLI signal and no aberrations in the bone and "S" in a white cell indicates aberrations in the skeletal bone but no BLI signal

NS no scans

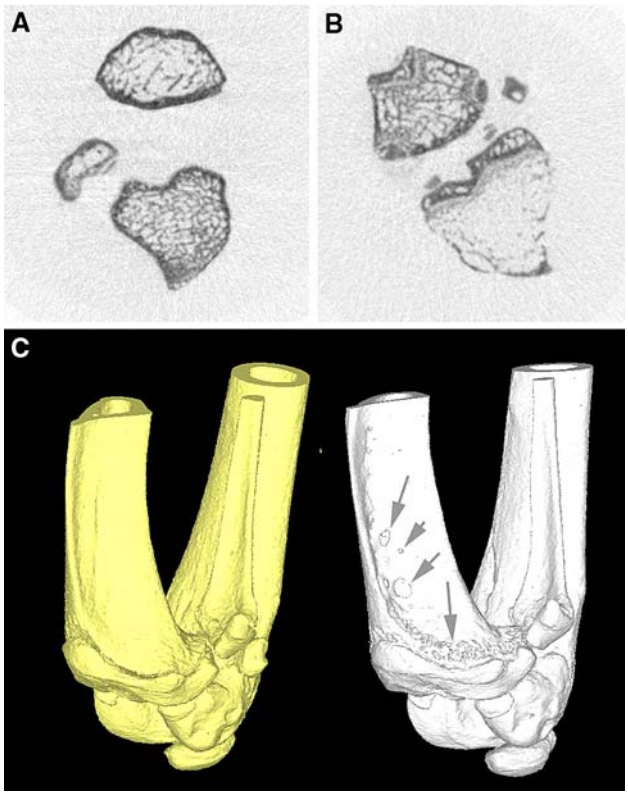

Fig. 2 Micro-CT analysis of the tibia (representative example). Pixel size is 13 µm. **a** Virtual cross section through control bone. **b** Cross section of MM bone. Notice the loss of trabecular bone mass and inner microarchitecture; the remaining bone is also less dense in the tibia from an MM mouse. **c** 3D reconstruction of a representative control (*left*) and an affected (*right*) tibia. *Arrows* indicate affected areas where cortical perforations are present

also became less dense. Figure 4 illustrates representative examples of outgrowth of bone in vertebrae as well as the presence of abnormal calcified tissue outside the ileum (bottom panel), probably resulting from periosteal reactions in the vicinity of tumors.

From these results it is obvious that micro-CT can image the final effect of the disease at the moment of death, i.e., abnormalities in the skeleton due to osteolytic lesions, but it cannot prove the presence of myeloma cells themselves. Therefore, these anatomical derangements were correlated with histological observations. This is illustrated in Figs. 5 and 6, where a semitransparent 3D model of the caudal part of the skeleton was reconstructed from virtual cross sections. The red areas indicate the structures that were affected by MM as detected by BLI. The inserts show the micro-CT sections, with arrows indicating bone defects. The histological sections and specific immune staining for myeloma cells (CD138 expression) confirm the presence of myeloma tumor cells at these locations, as shown in Fig. 6.

Histology

The presence of MM cells in the various bone specimens was confirmed by immunohistochemistry in detail in three mice. The findings were correlated with the aberrations of the skeleton detected by micro-CT (Table 2). Immunostaining is a sensitive method to show the presence of MM; also, small foci of MM cells can be detected, provided that the possible location of the tumor is identified, i.e., by BLI. Comparison of the BLI signal and the immunohistochemical confirmation yielded an overall correlation for 20 out of 23 specimens (Table 2). The histological slides also reveal lumbar vertebrae completely filled with MM tumor, with neighboring vertebrae that is completely normal (Fig. 6j, k). Even within a femur areas with MM and areas completely free of MM exist, again emphasizing the focal growth behavior of this MM line in the mouse model (Fig. 6a, l).

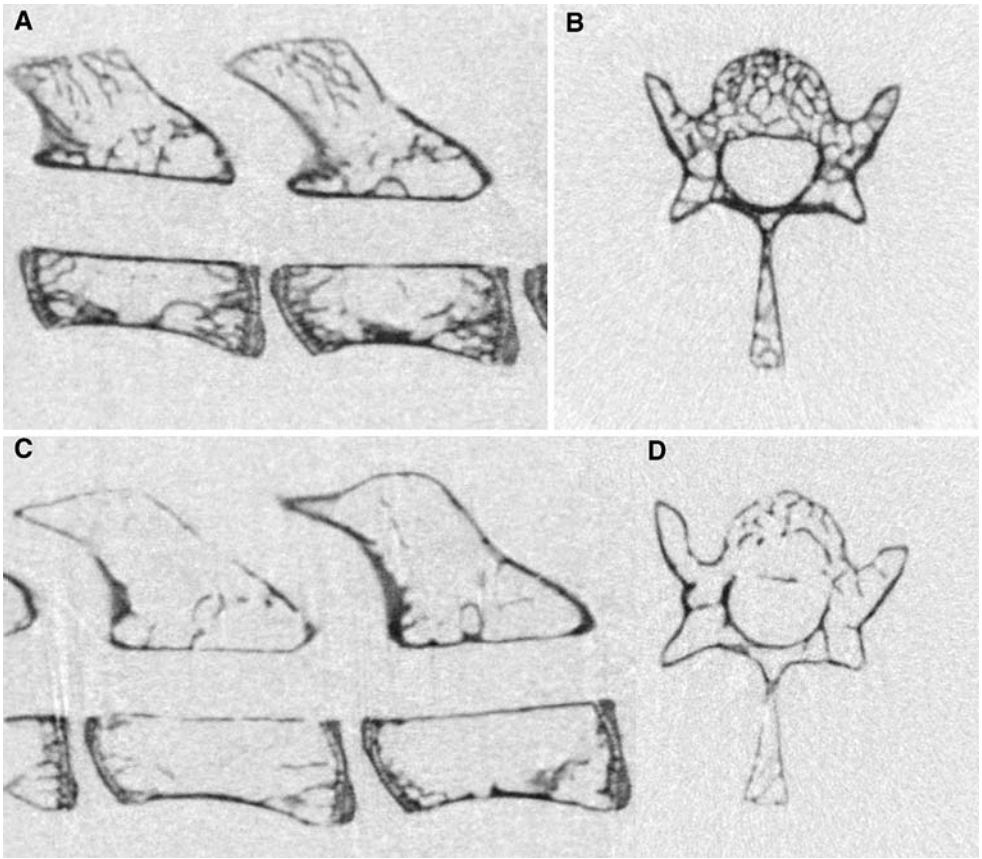

Fig. 3 Micro-CT analysis of the effect of MM on the vertebral column (representative example). Pixel size is 13 μm. **a**, **b** Two orthogonal sections through the vertebrae of a control animal are shown. **c**, **d** Two orthogonal sections through affected vertebrae of a diseased mouse, where loss of trabecular mass and architecture is present. Overall density of the remaining bone is smaller in MM

Discussion

The present study reports a multimodal imaging analysis of the effects caused by MM in immune-deficient mice. Initially, during a lifetime, outgrowth of myeloma cells was visualized by BLI. The brightness of the BLI signal is proportional to the tumor load. Therefore, this warrants the use of BLI to study the growth kinetics of MM and to validate experimental therapeutic interventions in this mouse model and underscores the value of imaging technology for this purpose reported by others [26, 27]. Analyzing the BLI images, we were able to localize the foci of MM growth in an area of a few millimeters in a bone. However, the presence of BLI signals indicates the presence of an MM tumor but it does not imply that the bone environment is damaged at this specific location, nor can it reveal the nature of the damage to the skeleton caused by the infiltrating tumor cells. The occurrence of bone lesions is a well-known symptom of MM, and therapeutic drugs, e.g., bisphosphonates, are prescribed [28] to block disease-induced osteoclast activity [29, 30], thus preventing osteolysis. In the humanized MM mouse model that uses human fetal bone implants to facilitate outgrowth of patient-derived primary MM cells, the bone resorbance by the myeloma cells is well described [31]. Whether these processes of osteolysis also occurred in our human MM cell lines based mouse model was unknown.

Previously, micro-CT was used to detect bone lesions in isolated tibiae in a murine model for MM [3]. In the present study full skeletons were scanned as an initial screening to determine the bones that were affected. Based on these results, isolated bones were scanned with a high-resolution and improved signal-to-noise ratio, resulting in more detailed images. The occurrence of osteolytic bone lesions (OBLs) in the human disease is associated with the presence of MM tumors and can be detected by CT analysis, as confirmed in this mouse model. The fact that micro-CT can be used to visualize this process is in agreement with reports from others [32, 33], but the combination of micro-CT with BLI that we studied has the option to follow the dynamics of these events during disease development as well as after therapy. In both micro-CT studies (full skeletons and isolated bones) we observed several defects in the diseased mice, which did not occur in normal control

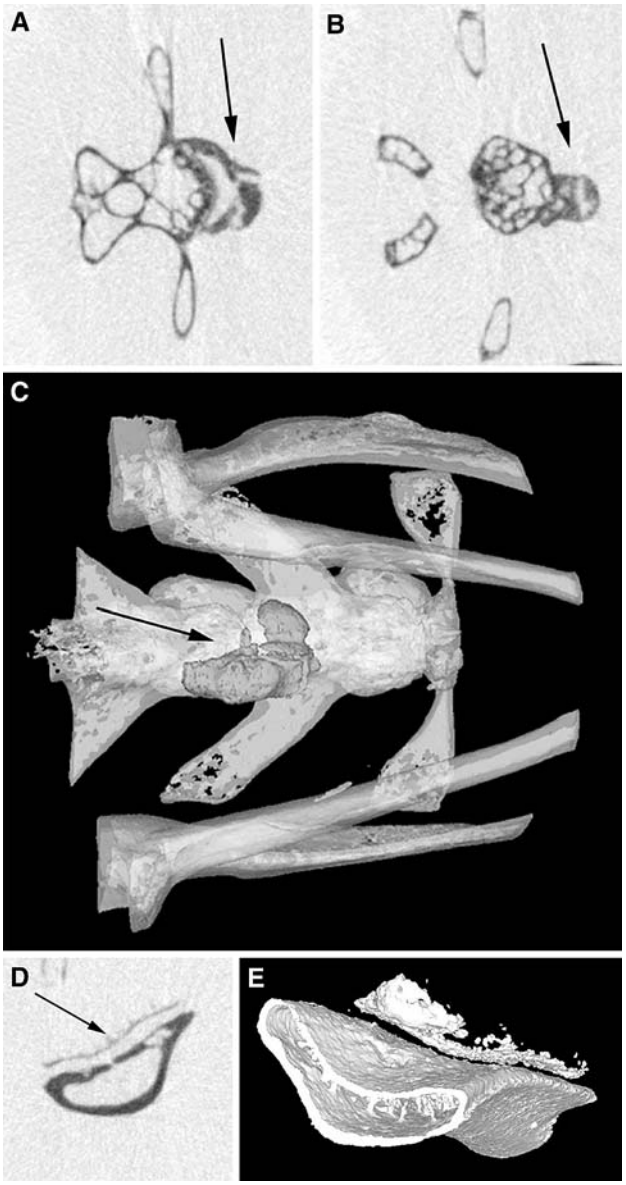

Fig. 4 External abnormal calcifications: calcified protuberance of a vertebra. Pixel size is 13 μm. **a**, **b** Representative cross sections showing the inner structure of the outgrowth. **c** 3D model. Outgrowth is indicated with an *arrow*. **d** (cross-section through the affected area) and **e** (3D model) Calcified tissue (*arrow*) that is formed close to the surface of the ilium, which is not observed in a healthy skeleton. Also notice the rough surface of the bone

mice, with comparable gender and age. After finishing the micro-CT experiments, the presence of MM tumors in the bones was confirmed by immunohistochemistry in three selected mice. In some cases foci of MM cells were present in the histological slices, although they had not caused any lesions that were detectable by micro-CT. One possible explanation for this discrepancy might be the fact that spatial resolution is lower in micro-CT than in histology and that the size of the lesions was too small for micro-CT. However, histology might miss some derangements due to the cutting bias. This latter phenomenon may also interfere while making a correlation between the results from the two techniques. In addition, the presence of regions of bone destruction as revealed by micro-CT was compared with the results previously obtained from BLI signals in living mice. When both BLI and micro-CT signals are positive, this observation implies that the MM cells caused their anatomical damage at the same locations where they were growing. This is the case in most of the regions, despite the fact that both signals were measured at different time points. In total 82% of all areas correlated (Table 1), with some skeleton parts having a higher correlation (sacrum and femora) and some skeleton parts having a lower correlation (sternum and humerus); but this is highly dependent on the high incidence of MM tumors present in those bones and unlikely to be statistically significant.

In the regions where the BLI signal was positive, no aberrations were observed by micro-CT. This might imply that the cells, although present, did not yet induce any visible anatomical destructions. We already discussed that probably a minimal amount of MM cells should be present for a certain period of time to cause some damage to the bone, which is a slow process. Areas with severe cortical bone defects (derangements as well as perforations), such as the sacrum and ileum in the pelvic area as well as the femora, were highly correlated with a strong BLI signal, indicative for a high tumor load.

The absence of a BLI signal combined with destruction seen by micro-CT might suggest that the MM cells secrete cytokines or other soluble factors that distribute throughout the circulation and may cause skeletal destruction (by stimulation of osteoclasts) not associated by cellular infiltration. In addition, the light absorption by tissues has been determined as a limitation to BLI sensitivity [26], which is therefore depth-dependent. Superficial small tumors can be as bright as deeply located large tumors. This may account for some differences in the observations from the two imaging techniques. In human disease the MM-associated OBL results from an uncoupling of osteoclast–osteoblast activity, in which factors, e.g., NFκB and osteoprotegerin (OPG), regulated by Wnt3a, play crucial roles [34]. On the other hand, dickkopf-1 (DKK-1) produced in cell lines or derived from bone marrow sera from MM patients, was reported to suppress Wnt-3-induced expression of OPG in osteoblasts [35]. The cell lines U266 and RPMI that we used constitutively produced a soluble Wnt inhibitor, secreted Frizzled-related protein 2 (sFRP-2), but not DKK-1 [35]. This opens up the possiblity of studying the anti-tumor potential of drugs that interfere with these pathways and how this affects the changes in the bone microenvironment. Another reason for us to establish a humanized MM model is in view of developing a model that would enable us to explore possibilities for adoptive immune

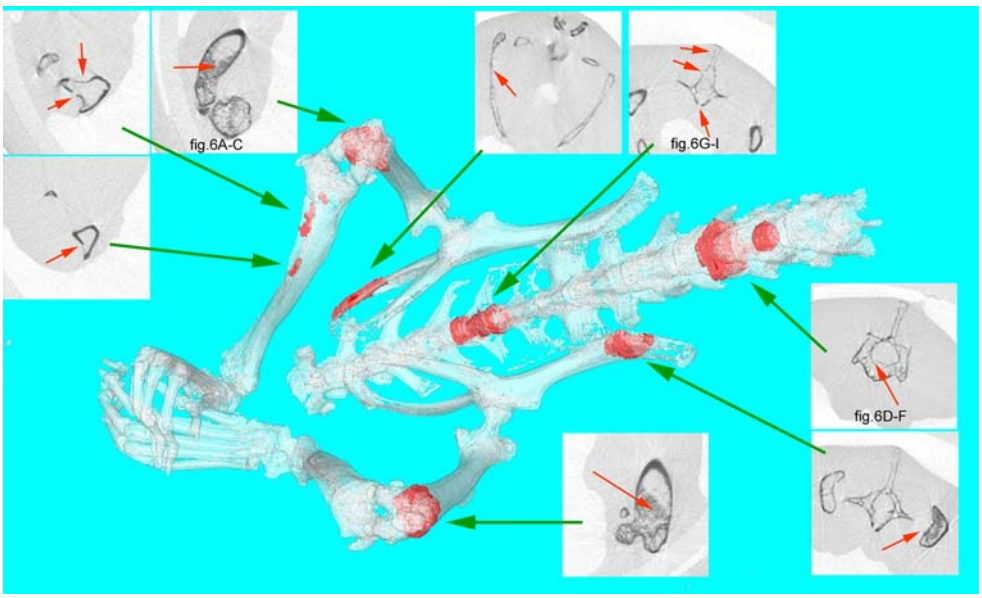

Fig. 5 Semitransparent 3D model of a mouse skeleton built from a full-body scan with 35 μm pixel size. Dark (*red*) areas in the skeleton indicates places affected by tumor activity. *Inserts* represent micro-CT sections with damaged bones. Letters correspond to histological sections shown in Fig. 6. (Color figure online)

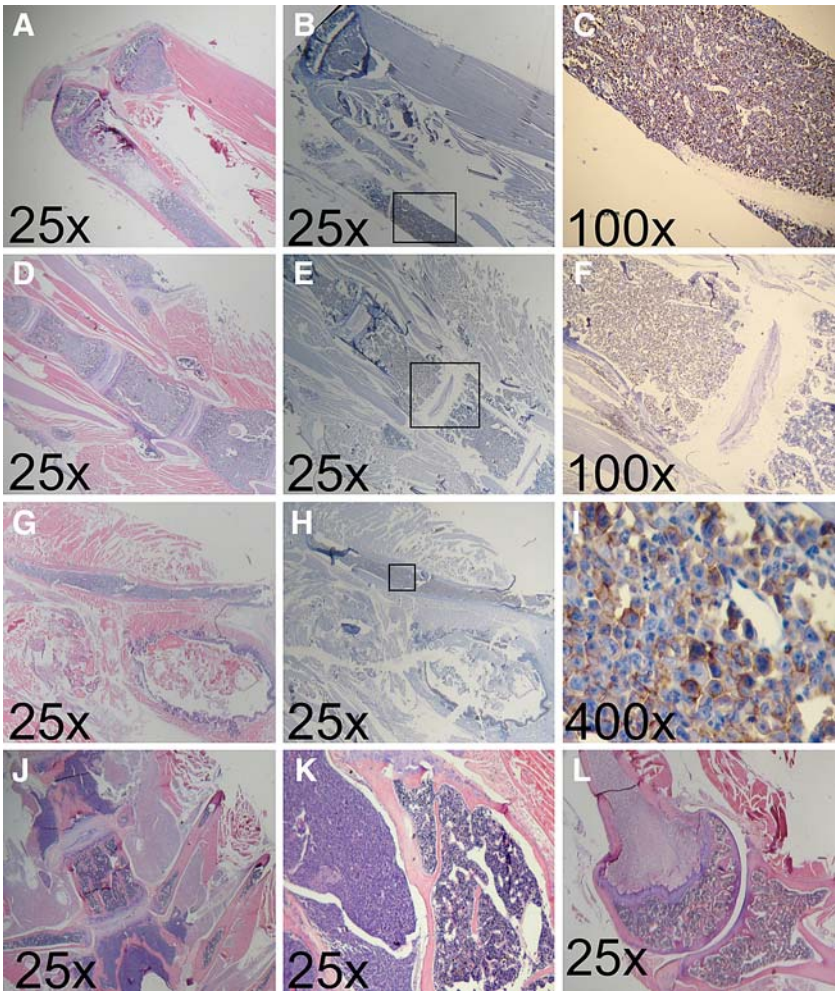

Fig. 6 Histology. Photographs of paraffin-embedded sections of various bones from the skeleton (femur, tibia, and vertebrae) of the mouse depicted in Fig. 5 (**a**–**i**), stained with hematoxylin–eosin (**a**, **d**, **g**, **j**, **k**, **l**) or after immunostaining for expression of CD138 antigen (**b**, **e**, **h**, **c**, **f**, **i**). **j**–**l** Examples of MM-diseased bones with adjacent bones displaying normal morphology. *Brown* (dark) color indicates the presence CD138-positive cells. Areas indicated by the squares in **b**, **e**, and **h** are enlarged in **c**, **f**, and **i**, respectively. Magnification is ×25 or ×400 as indicated. (Color figure online)

Table 2 Correlation of immunohistochemical detection of MM in specified bones with micro-CT-diagnosed aberrations

	Bones examined							
mouse #	L Femur	R Femur	lumbar vertebrae	thoracic vertebrae	sacral vertebrae	sacrum	L humerus	R humerus
9			M					M
11					M			
6							NH	

Three mice were analyzed in detail by immunohistochemistry. A gray cell in the table indicates a correlation in the presence of the MM cells diagnosed by immunohistochemistry and the micro-CT-detected aberrations in the specified bone. "M" in a black cell indicates the presence of MM cells and no micro-CT aberrations in the specified bone.

NH no histology could be performed because the bone was lost during preparation

therapy on the basis of minor HLA antigens (mHags) [36]. Certain mHags are exclusively expressed on patient hematopoietic and malignant cells that can be utilized for specific targeting of myeloma cells after human histocompatibility leukocyte antigen (HLA)–matched allogeneic stem cell transplantation (allo-SCT). Earlier we identified two mHags that can serve as targets for human cytotoxic T lymphocytes [5, 37]. Cloning of the corresponding T-cell receptor will open the possibility to further develop patient-tailored immunotherapy [7].

In summary, multimodal imaging analysis of human myeloma growth in the RAG2$^{-/-}\gamma c^{-/-}$ mouse revealed a clear correlation between the BLI signal, micro-CT analysis, and immunohistochemistry and in this respect strongly resembles the human disease. The model has potential for the study of the biology of human myeloma and for preclinical evaluation of new therapeutic approaches aimed at counteracting MM-induced bone lesions.

Acknowledgement The Micro-CT group thanks the IBBT TIRPA project and IWT SBO Quantiviam project (Prof. J. Sijbers, VisionLab, University of Antwerp) for financial support. Financial support was obtained from the Dutch Program for Tissue Engineering (DPTE-project 6729).

References

1. Kyle RA, Rajkumar SV (2008) Multiple myeloma. Blood 111: 2962–2972
2. Radl J, Croese JW, Zurcher C, Van den Enden-Vieveen MH, de Leeuw AM (1988) Animal model of human disease. Multiple myeloma. Am J Pathol 132:593–597
3. Libouban H, Moreau MF, Baslé MF, Bataille R, Chappard D (2003) Increased bone remodeling due to ovariectomy dramatically increases tumoral growth in the 5T2 multiple myeloma mouse model. Bone 33:283–292
4. Vanderkerken K, Asosingh K, Willems A, De Raeve H, Couck P, Gorus F, Croucher P, Van Camp B (2005) The 5T2MM murine model of multiple myeloma: maintenance and analysis. Methods Mol Med 113:191–205
5. Holloway PA, Kaldenhoven N, van Dijk M, Bloem AC, de Lau W, van der Zee R, Kircher-Eibl B, Mutis T, Lokhorst HM (2004) Susceptibility of malignant plasma cells to HA-1(H) specific lysis suggests a role for the minor histocompatibility antigen HA-1 in the graft-versus-myeloma effect. Leukemia 18:1543–1545
6. Spaapen R, van den Oudenalder K, Ivanov R, Bloem A, Lokhorst H, Mutis T (2007) Rebuilding human leukocyte antigen class II-restricted minor histocompatibility antigen specificity in recall antigen-specific T cells by adoptive T cell receptor transfer: implications for adoptive immunotherapy. Clin Cancer Res 13: 4009–4015
7. Dalton W, Anderson KC (2006) Synopsis of a roundtable on validating novel therapeutics for multiple myeloma (review). Clin Cancer Res 12:6603–6610
8. Feo-Zuppardi FJ, Taylor CW, Iwato K, Lopez MH, Grogan TM, Odeleye A, Hersh EM, Salmon SE (1992) Long-term engraftment of fresh human myeloma cells in SCID mice. Blood 80:2843–2850
9. Bellamy WT, Odeleye A, Finley P, Huizenga B, Dalton WS, Weinstein RS, Hersh EM, Grogan TM (1993) An in vivo model of human multidrug-resistant multiple myeloma in SCID mice. Am J Pathol 142:691–698
10. Reme T, Gueydon E, Jacquet C, Klein B, Brochier J (2001) Growth and immortalization of human myeloma cells in immunodeficient severe combined immuunodeficiency mice: a preclinical model. Br J Haematol 114:406–413
11. Urashima M, Chen BP, Chen S, Pinkus GS, Bronson RT, Dedera DA, Hoshi Y, Teoh G, Ogata A, Treon SP, Chauhan D, Anderson KC (1997) The development of a model for the homing of multiple myeloma cells to human bone marrow. Blood 90: 754–765
12. Yaccoby S, Barlogie B, Epstein J (1998) Primary myeloma cells growing in SCID-hu mice: a model for studying the biology and treatment of myeloma and its manifestations. Blood 92: 2908–2913
13. Pilarski LM, Hipperson G, Seeberger K, Pruski E, Coupland RW, Belch AR (2000) Myeloma progenitors in the blood of patients with aggressive or minimal disease: engraftment and self-renewal of primary human myeloma in the bone marrow of NOD SCID mice. Blood 95:1056–1065
14. Miyakawa Y, Ohnishi Y, Tomisawa M, Monnai M, Kohmura K, Ueyama Y, Ito M, Ikeda Y, Kizaki M, Nakamura M (2004) Establishment of a new model of human multiple myeloma using NOD/SCID/gammac(null) (NOG) mice. Biochem Biophys Res Commun 313:258–262
15. Mitsiades C, Mitsiades N, Munshi N, Anderson KC (2004) Focus on multiple myeloma. Cancer Cell 6:439–444
16. Huang SY, Tien HF, Su FH, Hsu SM (2004) Nonirradiated NOD/SCID-human chimeric animal model for primary human multiple

myeloma: a potential in vivo culture system. Am J Pathol 164:747–756
17. Tassone P, Neri P, Carrasco DR, Burger R, Goldmacher VS, Fram R, Munshi V, Shammas MA, Catley L, Jacob GS, Venuta S, Anderson KC, Munshi NC (2005) A clinically relevant SCID-hu in vivo model of human multiple myeloma. Blood 106:713–716
18. Yata K, Yaccoby S (2004) The SCID-rab model: a novel in vivo system for primary human myeloma demonstrating growth of CD138-expressing malignant cells. Leukemia 18:1891–1897
19. Ghosh N, Matsui W (2009) Cancer stem cells in multiple myeloma. Cancer Lett 277:1–7
20. Rozemuller H, Van der Spek, Bogers-Boer LH, Zwart MC, Verwey V, Emmelot M, Groen RW, Spaapen R, Bloem AC, Lokhorst HM, Mutis T, Martens AC (2008) A bioluminescence imaging based in vivo model for preclinical testing of novel cellular immunotherapy strategies to improve the graft-versus-myeloma effect. Haematologica 93:1049–1057
21. Weijer K, Uittenbogaart CH, Voordouw A, Blom B, Spits H (2002) Intrathymic and extrathymic development of human plasmacytoid dendritic cell precursors in vivo. Blood 99:2752–2759
22. Rozemuller H, Knaan-Shanzer S, Hagenbeek A, van Bloois L, Storm G, Martens AC (2004) Enhanced engraftment of human cells in RAG2/gammac double-knockout mice after treatment with CL2MDP liposomes. Exp Hematol 32:1118–1125
23. Paulus MJ, Gleason SS, Kennel SJ, Hunsicker PR, Johnson DK (2000) High resolution X-ray computed tomography: an emerging tool for small animal cancer research. Neoplasia 2:62–70
24. De Clerck NM, Meurrens K, Weiler H, Van Dyck D, Vanhoutte G, Terpstra P, Postnov AA (2004) High resolution X-ray microtomography for the detection of lung tumors in living mice. Neoplasia 6:374–379
25. Feldkamp LA, Davis LC, Kress JW (1984) Practical cone-beam algorithm. J Opt Soc Am A 1:612–619
26. Contag CH, Ross BD (2002) It's not just about anatomy; in vivo bioluminescence imaging as an eyepiece into biology. J Magn Reson Imaging 16:378–387
27. Mitsiades CS, Mitsiades NS, McMullan CJ, Poulaki V, Shringarpure R, Akiyama M, Hideshima T, Chauhan D, Joseph M, Libermann TA, García-Echeverría C, Pearson MA, Hofmann F, Anderson KC, Kung AL (2004) Inhibition of the insulin-like growth factor receptor-1 tyrosine kinase activity as a therapeutic strategy for multiple myeloma, other hematologic malignancies, and solid tumors. Cancer Cell 5:221–230
28. Rogers MJ, Watts DJ, Russell RGG (1997) Overview of bisphosphonates. Cancer 80:1652–1660
29. Coleman RE (2008) Risks and benefits of bisphosphonates. Br J Cancer 98:1736–1742
30. Smith RM (2008) Osteoclast targeted therapy for prostate cancer: bisphosphonates and beyond. Urol Oncol 26:420–425
31. Rabin N, Kyriakou C, Coulton L, Gallagher OM, Buckle C, Benjamin R, Singh N, Glassford J, Otsuki T, Nathwani AC, Croucher PI, Yong KL (2007) A new xenograft model of myeloma bone disease demonstrating the efficacy of human mesenchymal stem cells expressing osteoprotegerin by lentiviral gene transfer. Leukemia 21:2181–2191
32. Oyajobi BO, Muñoz S, Kakonen R, Williams PJ, Gupta A, Wideman CL, Story B, Grubbs B, Armstrong A, Dougall WC, Garrett IR, Mundy GR (2007) Detection of myeloma in skeleton of mice by whole-body optical fluorescence imaging. Mol Cancer Ther 6:1701–1708
33. Peyruchaud O, Winding B, Pécheur I, Serre CM, Delmas P, Clézardin P (2001) Early detection of bone metastases in a murine model using fluorescent human breast cancer cells: application to the use of the bisphosphonate zoledronic acid in the treatment of osteolytic lesions. J Bone Miner Res 16:2023–2027
34. Qiang YW, Chen Y, Stephens O, Brown N, Chen B, Epstein J, Barlogie B, Shaughnessy JD Jr (2008) Myeloma-derived Dickkopf-1 disrupts Wnt-regulated osteoprotegerin and RANKL production by osteoblasts: a potential mechanism underlying osteolytic bone lesions in multiple myeloma. Blood 112:196–207
35. Oshima T, Abe M, Asano J, Hara T, Kitazoe K, Sekimoto E, Tanaka Y, Shibata H, Hashimoto T, Ozaki S, Kido S, Inoue D, Matsumoto T (2005) Myeloma cells suppress bone formation by secreting a soluble Wnt inhibitor, sFRP-2. Blood 106:3160–3165
36. Goulmy E (1997) Human minor histocompatibility antigens: new concepts for marrow transplantation and adoptive immunotherapy. Immunol Rev 157:125–140
37. Spaapen RM, Lokhorst HM, van den Oudenalder K, Otterud BE, Dolstra H, Leppert MF, Minnema MC, Bloem AC, Mutis T (2008) Toward targeting B cell cancers with $CD4^+$ CTLs: identification of a CD19-encoded minor histocompatibility antigen using a novel genome-wide analysis. J Exp Med 205:2863–2872